Subtransus thermal route selection and constitutive assessment for Heat Stamping Ti-6Al-4V sheet

Famin Tian, Hao Wu and Nan Li*

Dyson School of Design Engineering, Imperial College London, Exhibition Road, South Kensington, London SW7 2DB, UK

* Corresponding author: n.li09@imperial.ac.uk

Abstract

Separating the soaking and deformation temperatures provides a means of tailoring the elevated-temperature response of Ti-6Al-4V sheet before rapid forming. Direct-heating (DH) and step-quenching (SQ) tensile responses were compared at subtransus temperatures and nominal strain rates of 0.1, 1 and 5 s^{-1}. SQ from 950 °C reduced the flow stress relative to DH at the same deformation temperature, but its effect on hardening and softening was strongly rate dependent. The 950→800 °C route exhibited prolonged hardening at 0.1 s^{-1} while retaining substantial softening at 5 s^{-1}. A 900→850 °C route provided a more balanced response, combining a lower flow stress than DH850 °C with reduced softening and positive apparent rate dependence. Post-test microscopy showed route- and rate-dependent α morphologies and image-derived α fractions consistent with the different thermal exposures and deformation times. A thermal-history-dependent constitutive formulation based on the Gavrus mixture framework was calibrated using the DH and 950 °C-based SQ datasets and subsequently assessed against the 900→850 °C route, capturing the principal stress, strain and rate trends over the calibrated strain range. A previously demonstrated cup with 1.8 draw ratio formed using the 900→850 °C route was further assessed at component level. The maximum measured thickness reduction was 12.7% near the punch corner. The simulation reproduced the overall thickness-profile trend and predicted considerable spatial variations in equivalent plastic strain and temperature during the 0.38 s draw. Post-form microscopy showed corresponding spatial changes in primary α morphology. The results identify the SQ900→850 °C route as a practical compromise within the tested matrix and demonstrate the importance of thermal history alongside instantaneous forming temperature and strain rate.

Keywords: Ti-6Al-4V; heat stamping; thermal history; viscoplasticity; phase transformation; finite element modelling.

1 Introduction

The elevated-temperature plastic response of Ti-6Al-4V depends not only on the instantaneous temperature, strain and strain rate, but also on the microstructure inherited from its thermal history, particularly the proportions and morphologies of the α and β phases established during heating and cooling and subsequently modified during deformation. The alloy combines high specific strength with properties suited to demanding structural applications, but the manufacture of complex sheet components remains constrained by forming cost and limited formability of titanium alloys [1][2][3][4]. Superplastic forming and conventional hot forming can accommodate complex geometries, although elevated-temperature processing and, particularly for superplastic forming, relatively low deformation rates can limit productivity [5][6][7][8][9][10][11].

Rapid forming of a heated blank with cooler tools offers an alternative route to titanium sheet components. Approaches involving resistance heating, rapid heating and modified hot stamping conditions have been investigated [12][13][14]. For Ti-6Al-4V, however, rapid forming introduces competing requirements. Deformation must proceed before excessive cooling restricts material flow, while local strain accumulation must remain sufficiently controlled to avoid severe thinning or fracture. Studies of Ti-6Al-4V hot stamping have identified a restricted temperature range in which components can be formed without surface cracking [14]. Temperature selection alone does not resolve this difficulty: the material response during forming is also affected by its phase constitution, prior thermal profile and the development of strain softening.

Strain hardening and positive strain-rate sensitivity both delay strain localisation [15][16][17][18][19]. Their relative importance can change with deformation conditions and microstructure evolution. Under superplastic conditions, grain-boundary sliding and its accommodation mechanisms can support large elongations, with the β phase facilitating deformation of the α grain assembly [20][21]. At the higher strain rates relevant to rapid stamping, substantial flow softening has been reported [14]. Reported contributions to flow softening include recovery and recrystallisation, phase transformation, globularisation, texture evolution and deformation-induced heating [22][23][24][25][26]. Several of these mechanisms may act concurrently, and their influence depends on the starting structure and processing conditions. A forming route therefore needs to balance the reduction of flow stress against the retention of sufficient hardening and positive rate dependence to limit localisation.

Tian and Li [27] previously proposed the Heat Stamping (HS) process, in which a step-quenching (SQ) treatment separates the temperature used to establish the predeformation microstructure from

the temperature at which stamping begins. A blank is soaked at a higher temperature and rapidly cooled to a lower deformation temperature before forming. In contrast, a direct-heating (DH) route brings the material to the deformation temperature without this preceding soak at a higher temperature. For Ti-6Al-4V, these routes can produce different phase populations and different transient responses at the same nominal deformation temperature. The effectiveness of this approach consequently depends on both the soaking and deformation temperatures and the time available for microstructural change.

Controlled thermal histories have been explored as a means of modifying the forming response of Ti-6Al-4V. The FAST process uses rapid heating to establish a non-equilibrium microstructure before forming [13]. Initial feasibility work on HS [27] reported tensile behaviour for the 950→800 °C route and demonstrated cup forming. Wu et al. [28] subsequently reported cups with draw ratios up to 1.8, together with post-forming hardness and springback measurements. The present study builds on this earlier work through a broader comparison of subtransus thermal routes, constitutive modelling of the route-dependent tensile response, and component-level assessment of the selected 900→850 °C route.

Constitutive modelling and microstructural evolution during hot deformation of Ti-6Al-4V have been extensively studied [23][29][30][31]. Martin et al. [32] coupled phase-transformation kinetics with Ti-6Al-4V rheology after supertransus heating followed by cooling to subtransus deformation temperatures. Gao et al. [33] incorporated heating-rate effects into a viscoplastic formulation assessed using current-assisted stamping, while Cai et al. [34] considered the transfer of internal material states through multistage Ti-6Al-4V forming. The question here is more specific: how a subtransus soak followed by step quenching changes the flow stress, hardening/softening behaviour and apparent rate dependence, and whether a constitutive description can represent the corresponding response during rapid drawing. Conventional constitutive laws expressed only in terms of the current strain, strain rate and temperature cannot distinguish thermal histories that arrive at the same instantaneous state [35][36][37][38], motivating the inclusion of thermal-history-dependent state terms.

A component-level comparison is also needed because agreement with tensile curves alone does not establish how a constitutive description performs during drawing. Cup forming combines bending, unbending, stretching and circumferential compression, while contact with the colder tools produces spatial temperature gradients. The thickness distribution provides a direct measure of local thinning and thickening, whereas the post-form microstructure provides complementary evidence of spatially heterogeneous deformation and thermal evolution. Comparison with the predicted strain and

temperature fields can therefore help relate the tensile response to material redistribution in the formed component.

The study therefore first compares the DH and SQ tensile responses and their associated post-test microstructures, before selecting the 900→850 °C route from the tested matrix on the basis of flow stress, hardening/softening behaviour and apparent rate dependence. A thermal-history-dependent constitutive formulation based on the framework of Gavrus [39] is then calibrated using the DH and 950 °C-based SQ data and assessed against the additional 900→850 °C route. Finally, the selected route is examined at component level using the cup thickness distribution, predicted strain and temperature fields, and post-form microstructure. The experimental and computational programme was originally documented in the thesis [40], while previously reported process feasibility retains its original attribution [27][28].

2 Materials and methods

2.1 Material and thermal routes

The material was Ti-6Al-4V sheet with a thickness of 1.6 mm and a reported β-transus temperature of 995 °C. Its chemical composition was 6.062 Al, 4.090 V, 0.115 Fe, 0.006 C, 0.030 N, 0.176 O and 0.004 H, in wt.%, with Ti as the balance. The as-received microstructure comprised equiaxed primary α (α_p) grains and intergranular β. Dog-bone tensile specimens were laser cut along the rolling direction. The parallel section was 30 ± 0.5 mm long and 6 ± 0.05 mm wide; the overall length was 100 mm and the shoulder radius was 5 mm.

Two thermal routes were compared namely direct heating (DH) and step quenching (SQ). For DH, specimens were heated at 25 °C s^{-1} to the deformation temperature and held for 300 s before tension. For SQ, specimens were heated at the same rate to a soaking temperature, T_S, held for 300 s, and cooled at 50 °C s^{-1} by compressed air to a lower deformation temperature, T_D, before tension. All soaking temperatures were below the β-transus. The SQ route was designed to alter the phase state entering deformation independently of the deformation temperature, thereby reproducing the principal thermal sequence of the Heat Stamping process.

The rate-dependent tensile matrix comprised DH at 800, 850, 900 and 950 °C and SQ at 950→800 °C and 950→900 °C, tested at nominal strain rates of 0.1, 1 and 5 s^{-1}. A further SQ900→850 °C route was tested at the same three rates to examine a lower soaking temperature and a smaller soaking-to-deformation temperature interval.

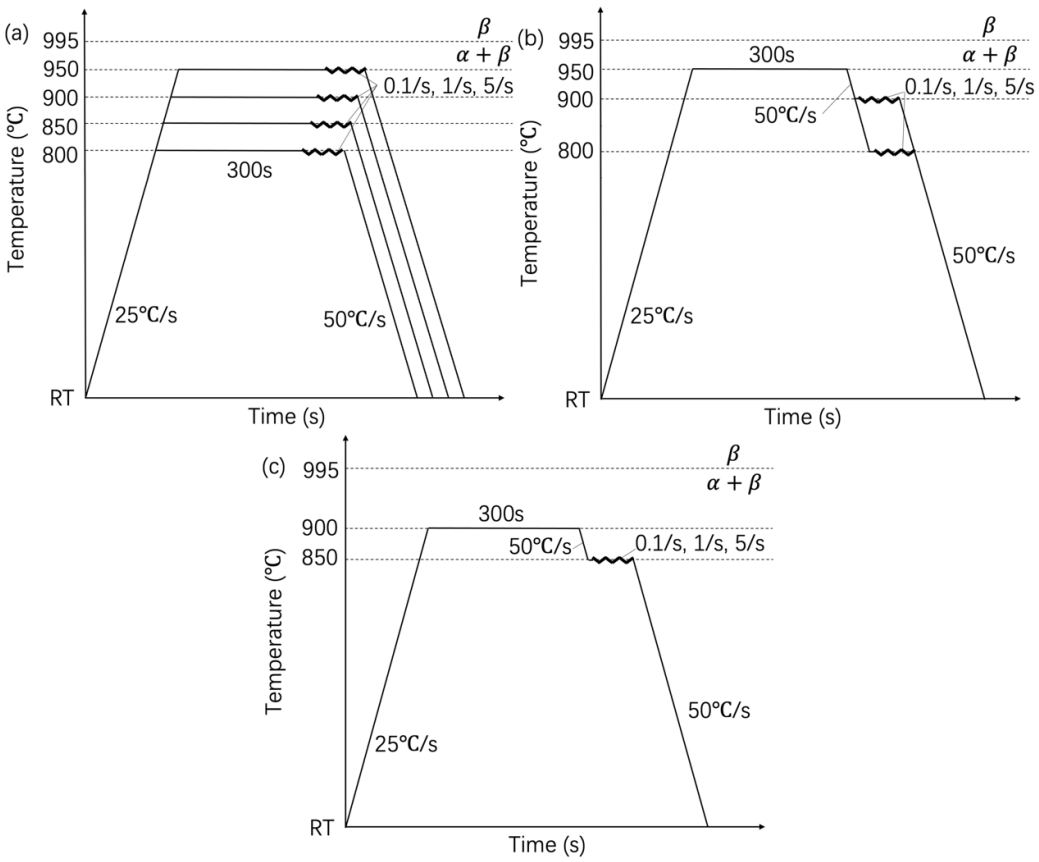


Figure 1. Programmed temperature histories for uniaxial tension: (a) direct heating; (b) step quenching from 950 °C; and (c) step quenching from 900 to 850 °C. The schematic specifies heating and cooling rates of 25 and 50 °C s^{-1} and a 300 s soak. Note that the deformation segments are schematic and do not represent the actual deformation duration or strain. All specimens were deformed to fracture before cooling.

2.2 Tensile testing and contactless strain measurement

High-temperature tensile tests used a Gleeble 3800 thermomechanical simulator, with direct resistance heating and compressed-air cooling. Figure 2 shows the detailed experimental setup for the tests. K-type thermocouples were welded at the centre of the gauge section for temperature measurement and control. Tests were conducted in ambient air. Force was measured at the fixed jaw. Fractured specimens were rapidly cooled to room temperature for microstructural examination.

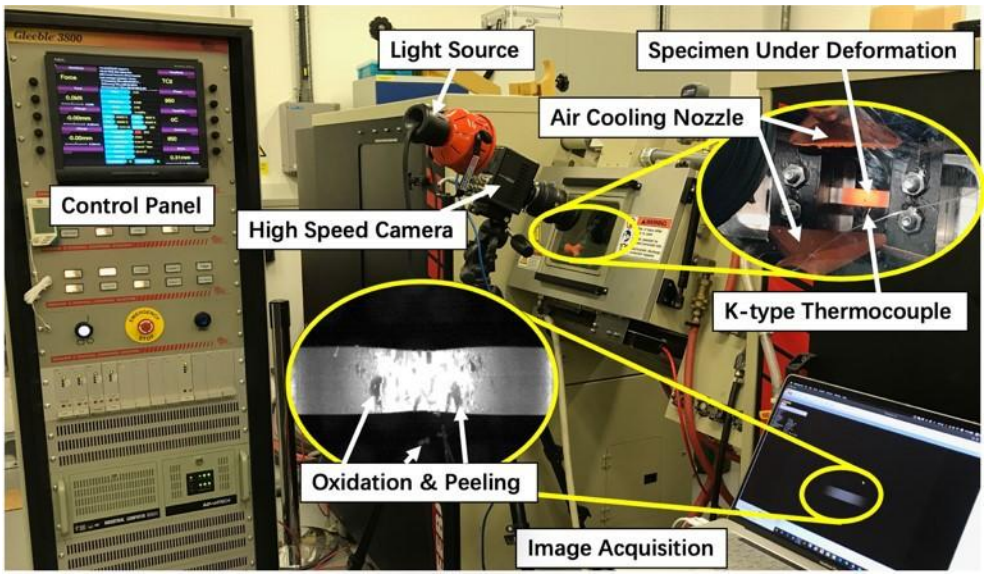


Figure 2. Experimental setup of high temperature tensile tests using a Gleeble 3800 system.

Axial strain was estimated from the local width evolution recorded by high-speed imaging to avoid heat loss associated with a contacting extensometer. Surface oxidation and oxide-layer detachment also made stable speckle tracking difficult under the present conditions [41][42][43]. To improve the contrast at the specimen edges, the optical arrangement used a black background behind the specimen and an additional light source (Figure 2). Image acquisition rates were 50, 500 and 1000 frames s^{-1} for tests at nominal strain rates of 0.1, 1 and 5 s^{-1}, respectively.

The recorded video was separated into frames and rotated to align the initial upper specimen edge horizontally. A Sobel filter detected the upper edge from the grey-level gradient [44]. Discontinuities associated with oxide cracking were screened against adjacent pixels and interpolated. The lowest upper-edge position defined a local search of the lower edge within ±3 pixels; the edge separation gave the local width W. The width signal was converted to strain using the method cited by Li et al. [15] and smoothed with a 30-frame Gaussian-weighted moving average [45]. Optical and force records were aligned at complete fracture. Assuming negligible volume change and approximately equal logarithmic contraction in the width and thickness directions, the local axial logarithmic strain was estimated as $\varepsilon \approx -2\ln(W/W_0)$. Under the same approximation, $A/A_0 \approx (W/W_0)^2$, giving $\sigma \approx F/[A_0 (W/W_0)^2]$. Here, W_0 and A_0 are the initial width and cross-sectional area, respectively, and F is the measured tensile force. The width-derived quantity therefore represents a local axial strain estimate. After localisation, the assumptions of equal transverse contraction and uniaxial stress become less representative. The fixed 30-frame smoothing window corresponds to nominal strain spans of approximately 0.06, 0.06 and 0.15 at 0.1, 1 and 5 s^{-1}, respectively.

2.3 Microstructural characterisation

Samples for microstructural analysis were sectioned using an abrasive cut-off machine, hot mounted and ground using P800, P1200, P2500 and P4000 SiC papers. Final polishing used colloidal silica suspension supplemented with a 30% hydrogen peroxide solution. A Tescan Clara scanning electron microscope was operated in backscattered-electron (BSE) mode to examine phase morphology, and ImageJ was used to determine image-derived α fractions. The reported α fraction was taken as the combined fraction of primary α and resolved globular secondary α ($\alpha_p + \alpha_s$) [40]. Primary α denotes the pre-existing globular grains, while secondary α denotes the additional globular features identified within the transformed β constituent.

2.4 Cup component forming setup

Circular Ti-6Al-4V blanks, initially 2.56 mm thick, were drawn at ratios of 1.6, 1.7 and 1.8, defined as blank radius divided by punch radius. The 2.56 mm forming blanks were supplied in the same material condition as the sheet used for tensile characterisation. Blanks were cut by electrical discharge machining and the sides were ground using P2500 SiC paper. The original tooling drawing [40] specifies an 80 mm punch diameter, an 86.14 mm die bore and an 85.5 mm blankholder bore. The corresponding radial gaps are 3.07 and 2.75 mm; the former exceeds the initial sheet thickness by approximately 20%. Punch and die entry radii were 10 and 15 mm, respectively, and the spacer height was 2.94 mm. The tools had zero draft angle and used H13 steel heat treated to HRC 45-50. The forming toolset was installed on a rig mounted on a 250 kN hydraulic press.

Boron nitride was applied to both blank surfaces and dried for 30 min before heating, to limit oxidation and facilitate material flow during forming. A graphite-based anti-seize lubricant was applied to the punch to facilitate removal of the formed components. Each blank was soaked at 900 °C for 5 min, transferred from the furnace to the blankholder in approximately 3 s, and cooled to 850 °C using a closed-loop compressed-air quenching system. A grounded K-type thermocouple embedded through the blank edge was used to monitor the blank temperature in real time. Separate control of the inner and outer regions allowed the airflow to be adjusted according to their different cooling responses, while spring plungers supported the blank at discrete contact points to limit conductive cooling before forming. The tools were initially at approximately 22 °C.

The quenching system used an axisymmetric nozzle arrangement to apply compressed air across the blank. Peripheral airflow was delivered through four adjustable nozzle groups, each covering approximately one quarter of the flange region, and a separate nozzle supplied the inner region.

Proportional solenoid valves regulated the flow under temperature feedback. The controller tracked the prescribed step-quenching temperature profile and stopped quenching when the designated forming temperature was reached. The onset of deformation was recorded using an accelerometer on the press fixture, providing an indication of first contact between the die and blankholder. This arrangement allowed the selected thermal route to be applied immediately before rapid drawing.

Drawing began at a nominal blank temperature of 850 °C, with a nominal 75 kN blankholding load and a ram speed of 200 mm s^{-1}. The descending die clamped the blank and drew it over the stationary punch. The reported deformation interval was 0.38 s, after which the component cooled on the punch.

After forming, the draw-ratio-1.8 cup was sectioned in the RD-ND plane. Thickness was measured at 5 mm intervals along the component profile and normalised by the initial 2.56 mm blank thickness. Post-form BSE observations were obtained at the bottom, wall and flange locations A, F and H and at the inner, central and outer punch-corner positions d_i, d_c and d_o shown later in Figure 11.

2.5 Thermomechanical finite element model

An axisymmetric coupled thermomechanical model of the draw-ratio-1.8 cup was developed in Abaqus/Explicit (Figure 3). The blank and tools were represented using CAX4RT coupled temperature-displacement elements. The constitutive formulation described in Section 4 was implemented through a VUMAT using isotropic J2 plasticity and a Newton-Raphson return-mapping scheme [46]. The punch was fixed and the die moved downward at 200 mm s^{-1}. A uniform pressure of 2.92 MPa represented the nominal 75 kN blankholding load, and an initial 0.38 mm blankholder separation represented the spring-plunger support prior to clamping. The blank and tools were initialised at 850 and 22 °C, respectively; furnace heating, transfer and step quenching were therefore not simulated explicitly. The principal forming and finite-element inputs are summarised in Table 1.

Table 1. Forming conditions and principal finite-element inputs.

Quantity	**Value**
Initial blank thickness	2.56 mm
Draw ratios tested	1.6, 1.7 and 1.8
Draw ratio simulated	1.8
Punch diameter / corner radius	80 / 10 mm
Die entry radius	15 mm
Soaking temperature / time	900 °C / 5 min
Forming temperature / initial tool temperature	850 / 22 °C
Nominal blankholding force	75 kN
Ram speed / deformation interval	200 mm s^{-1} / 0.38 s
Element type	CAX4RT, coupled axisymmetric temperature-displacement
Blank element size	0.28 mm; approximately 9 elements through thickness
Tool contact-layer depth / nominal body mesh	5 mm / 1.25 mm
Friction coefficient / Taylor-Quinney coefficient	0.2 / 0.5
Die bore / holder bore	86.14 / 85.50 mm
Die / holder radial gap	3.07 / 2.75 mm
Spacer height	2.94 mm

A blank element size of 0.28 mm provided approximately nine elements through the sheet thickness. Tool regions within 5 mm of the contact surfaces were locally refined, while the nominal tool-body element size was 1.25 mm. A finer blank mesh of 0.21 mm produced only a small change in the monitored thickness response, and the 0.28 mm mesh was therefore retained for the component simulation. Figure 3 shows the model geometry, boundary conditions and local mesh refinement.

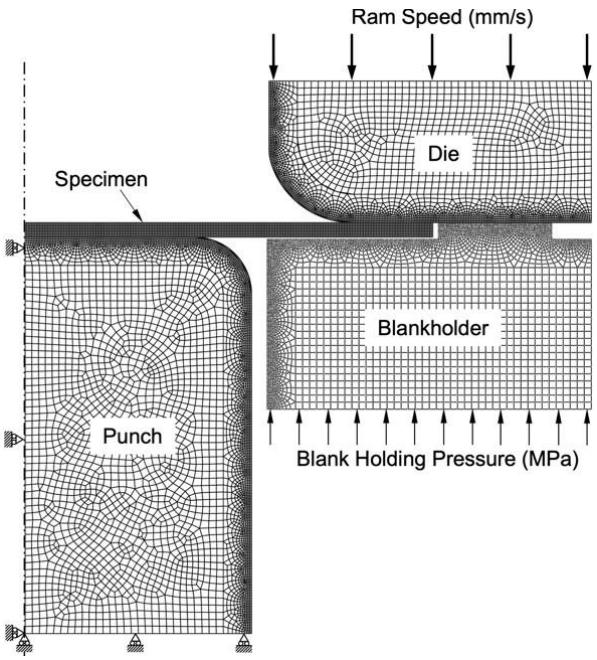


Figure 3. Axisymmetric finite-element representation of the Heat Stamping experiment, showing the blank, punch, die and blankholder, boundary conditions and local mesh refinement.

Temperature-dependent elastic and thermal properties were assigned to Ti-6Al-4V. Young's modulus was defined as $E = 0.86 \exp(3521.44/T)$ GPa, with T in kelvin, over the temperature range considered [47][48][49]. The Poisson ratio and density were 0.34 and 4430 kg m^{-3}, respectively. The H13 tools were assigned a Young's modulus of 210 GPa, Poisson ratio of 0.30, density of 7800 kg m^{-3}, thermal conductivity of 24.4 W m^{-1} K^{-1}, and specific heat capacity of 460 J kg^{-1} K^{-1}. The temperature-dependent thermal conductivity and heat capacity of Ti-6Al-4V are listed in Table 2. Plastic-work conversion to heat was represented using a Taylor-Quinney coefficient of 0.5 [50].

Table 2. Temperature-dependent thermal properties of Ti-6Al-4V used in the forming simulation [47].

Temperature (°C)	**Thermal conductivity (W m^{-1} K^{-1})**	**Specific heat capacity (J kg^{-1} K^{-1})**
204	8.65	601.42
315	10.38	629.72
427	11.94	669.81
538	13.67	728.77
649	14.88	797.17
760	16.61	896.23
871	17.99	983.49
958	17.99	983.49

Contact between Ti-6Al-4V and H13 used the pressure-dependent interfacial heat-transfer coefficients listed in Table 3 [47][51], together with a gap conductance of 0.7 kW m^{-2} K^{-1} and a friction coefficient of 0.2 [47]. Convection and radiation were neglected during the 0.38 s drawing interval. The coupled analysis therefore accounts for both heat generation by plastic deformation and conductive heat transfer from the heated blank to the colder tooling.

Table 3. Pressure-dependent interfacial heat-transfer coefficient between Ti-6Al-4V and H13 used in the forming simulation [47][51].

Contact pressure (MPa)	**Interfacial heat-transfer coefficient (kW m^{-2} K^{-1})**
0	0.95
15	2.80
30	3.94
45	4.65
60	5.08
90	5.52
120	5.68
150	5.74

3 Thermal-route-dependent plasticity

3.1 Flow stress and the effect of step quenching

Figure 4 compares the DH responses at 800, 900 and 950 °C with the SQ950→800 °C and SQ950→900 °C responses at the three strain rates. Deformation temperature affected both the stress level and the shape of the flow curves. For DH, the 800 °C response showed an initial hardening stage at 1 and 5 s^{-1}, followed by flow softening, whereas the 900 and 950 °C curves showed more pronounced softening. Across the DH conditions shown, the recorded terminal strain generally decreased with increasing strain rate.

On the other hand, SQ changed the response at a given deformation temperature. Peak stresses after SQ were lower than those after DH at the corresponding temperature. SQ at 950→800 °C produced a higher recorded terminal strain than DH at 800 °C, but its effect on the subsequent stress evolution depended strongly on rate. At 0.1 s^{-1}, the SQ curve exhibited prolonged hardening up to a true strain of approximately 0.4. At 1 s^{-1}, softening was reduced over part of the strain range. At 5 s^{-1}, however, however, significant post-peak softening remained. Consequently, a reduction in flow stress alone did not identify a uniformly favourable forming route.

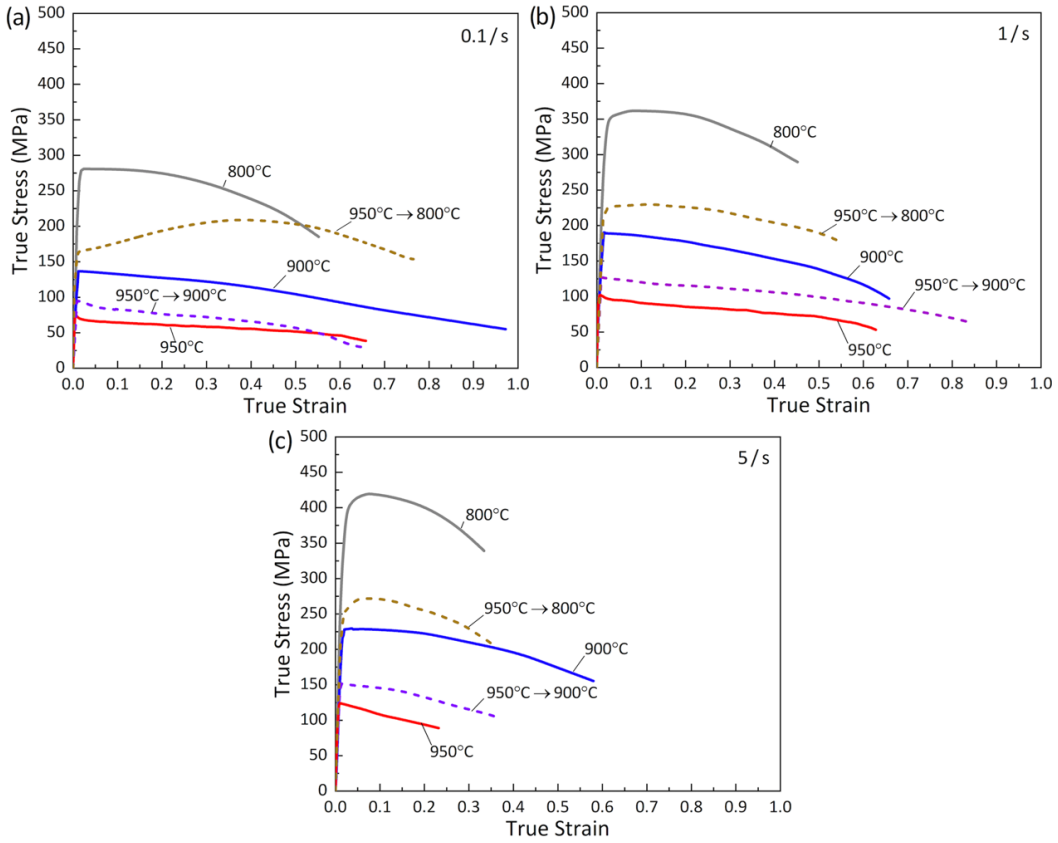


Figure 4. Comparison of true stress-strain curves after DH at 800, 900 and 950 °C and SQ at 950→800 °C and 950→900 °C, at strain rates of (a) 0.1, (b) 1 and (c) 5 s^{-1}.

The response at 950→900 °C was also rate dependent. At 1 s^{-1}, SQ950→900 °C showed reduced softening and a higher recorded terminal strain than DH900 °C. At 0.1 and 5 s^{-1}, the SQ curves instead exhibited substantial softening and lower recorded terminal strains than the corresponding DH curves. These comparisons show that the benefit of SQ cannot be specified solely by the difference between soaking and deformation temperatures; it also depends strongly on deformation rate.

The strain dependence of the response was quantified using the normalised hardening rate, γ' [52]:

$$\gamma' = \frac{\partial \ln \sigma}{\partial \varepsilon} = \frac{1}{\sigma}\frac{\partial \sigma}{\partial \varepsilon} \quad (1)$$

Here σ and ε denote the reported true stress and width-derived axial strain, respectively. Positive and negative γ' indicate hardening and softening, respectively. At 1 s^{-1}, the 950→800 °C route showed less softening than DH at 800 °C over the later part of the analysed range, while 950→900 °C reduced softening relative to DH at 900 °C. Neither SQ route reduced the displayed softening at 5 s^{-1}.

Hardening and apparent rate dependence describe different aspects of the measured behaviour. A curve with a lower stress level can nevertheless soften more rapidly with strain, while strong low-rate hardening does not necessarily correspond to strong positive apparent rate sensitivity. Both characteristics therefore need to be considered when selecting a route for stamping. The 950→800 °C results illustrate this distinction: the extended low-rate hardening stage would, in isolation, tend to resist strain localisation, whereas the accompanying high-rate softening reduces the stress separation between rates as strain accumulates.

3.2 Microstructural observations and interpretation

Figure 5 compares the post-test microstructures after DH950 °C, SQ950→900 °C and SQ950→800 °C. After DH950 °C, the microstructure comprised primary α and a transformed β constituent containing acicular α. After SQ, globular features identified as secondary α were observed within the transformed β regions. Their prominence varied with thermal route and strain rate; for SQ950→900 °C such features were less evident in the displayed 5 s^{-1} field, whereas secondary α features remained visible across the SQ950→800 °C conditions shown. The final post-test morphology reflects both the deformation stage and subsequent cooling.

Rapid cooling from the soaking temperature was intended to retain a β-rich non-equilibrium state relative to equilibrium at the lower deformation temperature. Previous studies have shown that cooling history and supersaturation influence secondary α nucleation and growth in two-phase titanium alloys [53][54][55]. Deformation-generated dislocations, grain boundaries and subgrain boundaries in the β constituent can provide potential nucleation sites [56], while defect-assisted transport has also been considered in descriptions of Ti-6Al-4V deformation and globularisation [57]. The observed globular features are therefore consistent with secondary α formation and deformation-assisted morphological evolution.

Several contributions may compete during deformation. Primary α generally offers greater resistance to plastic flow than β, and strain incompatibility between the phases can promote dislocation accumulation [21][23]. If secondary α develops during deformation, it may contribute to maintaining the flow stress, whereas recovery and recrystallisation reduce stored dislocation content and contribute to softening [58]. Reaching a nominal strain of 0.2 requires approximately 2, 0.2 and 0.04 s at 0.1, 1 and 5 s^{-1}, respectively. The greater prominence of globular secondary α after the lower-rate SQ tests is therefore consistent with the longer time available for microstructural evolution. Deformation heating may provide an additional contribution at higher rates [59].

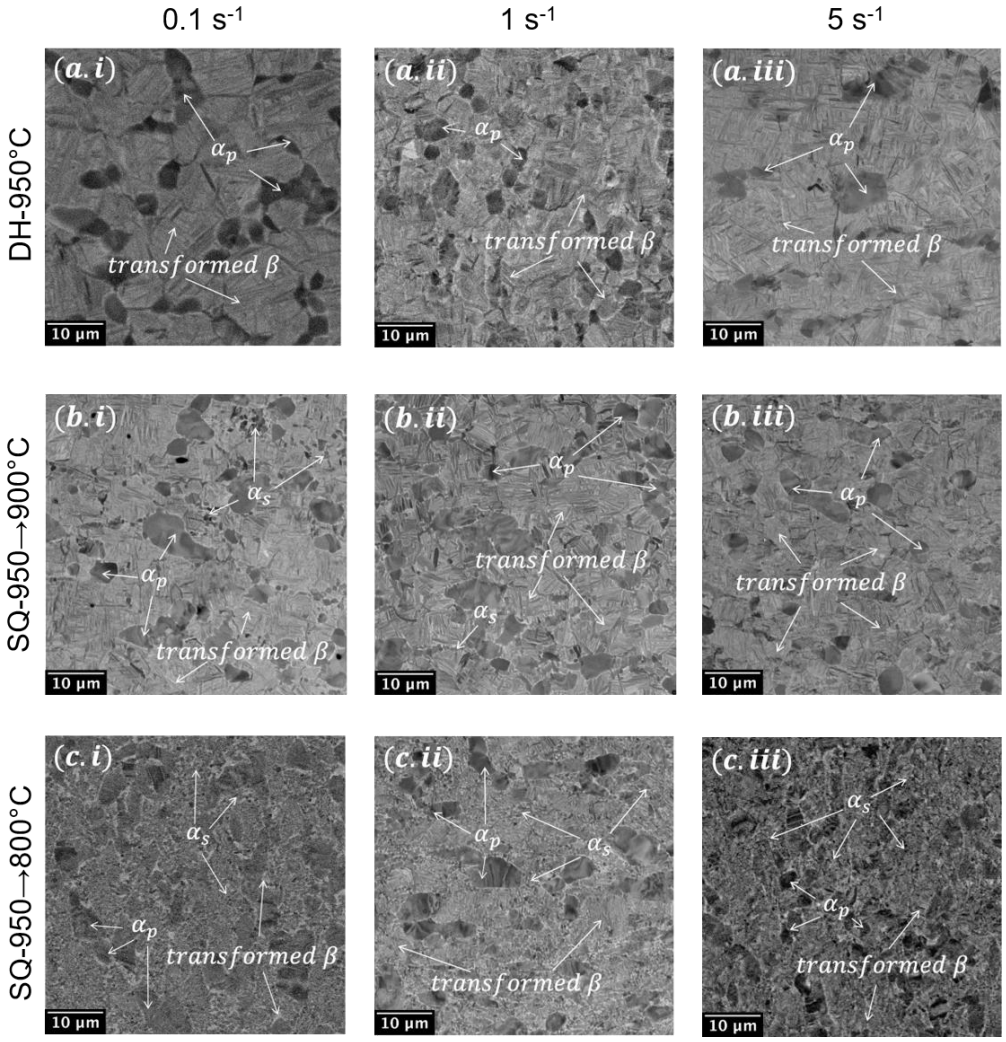


Figure 5. Post-test microstructures after (a) DH at 950 °C, (b) SQ at 950→900 °C and (c) SQ at 950→800 °C. Columns (i), (ii) and (iii) correspond to strain rates of 0.1, 1 and 5 s^{-1}, respectively.

A further proposed contribution concerns deformation heating. At high rates, plastic work can raise the local temperature [59] and favour $\alpha \rightarrow \beta$ transformation during DH [24]. For SQ, the higher soaking temperature establishes a different initial phase balance. If the material retains that balance during cooling and its temperature during deformation remains below the soaking temperature, the driving force for further primary α dissolution may be reduced.

3.3 Selection and assessment of the 900→850 °C deformation route

The routes discussed above starting at 950 °C revealed a trade-off: 950→900 °C retained substantial softening, while 950→800 °C combined low-rate hardening with high-rate softening and consequently reduced stress separation between rates as strain accumulated. A further route, 900→850 °C, was investigated to start deformation from a state expected to retain more primary α than after soaking at 950 °C while preserving a difference between soaking and deformation

temperatures. This route was therefore examined as an experimentally accessible compromise among flow stress, resistance to softening and positive apparent rate dependence.

Figure 6 compares the SQ900→850 °C response with DH at 850 and 900 °C across all three nominal strain rates. At each strain rate, the SQ900→850 °C response lay between the DH850 °C and DH900 °C responses over the initial strain range up to approximately 0.2. Relative to DH at 850 °C at the same nominal rate, the 900→850 °C route showed reduced flow softening in the displayed comparisons (Figure 6). At 0.1 and 1 s^{-1}, the 900→850 °C curves remained approximately level or hardened over much of the interval up to a reported true strain of 0.2. At 5 s^{-1}, the SQ900→850 °C curve retained an initial hardening stage before subsequent softening.

Rate dependence was described by a linear fit of ln σ against ln $\dot{\varepsilon}$ across the three nominal rates at fixed reported strain. Equation 2 defines the strain-rate sensitivity used here. m' was obtained from the slope fitted to the three constant-rate tests at a given strain, so it represents an apparent rate dependence across separate tests rather than an instantaneous material response:

$$m' = \frac{\partial \ln \sigma}{\partial \ln \dot{\varepsilon}} = \frac{\dot{\varepsilon}}{\sigma}\frac{\partial \sigma}{\partial \dot{\varepsilon}} \tag{2}$$

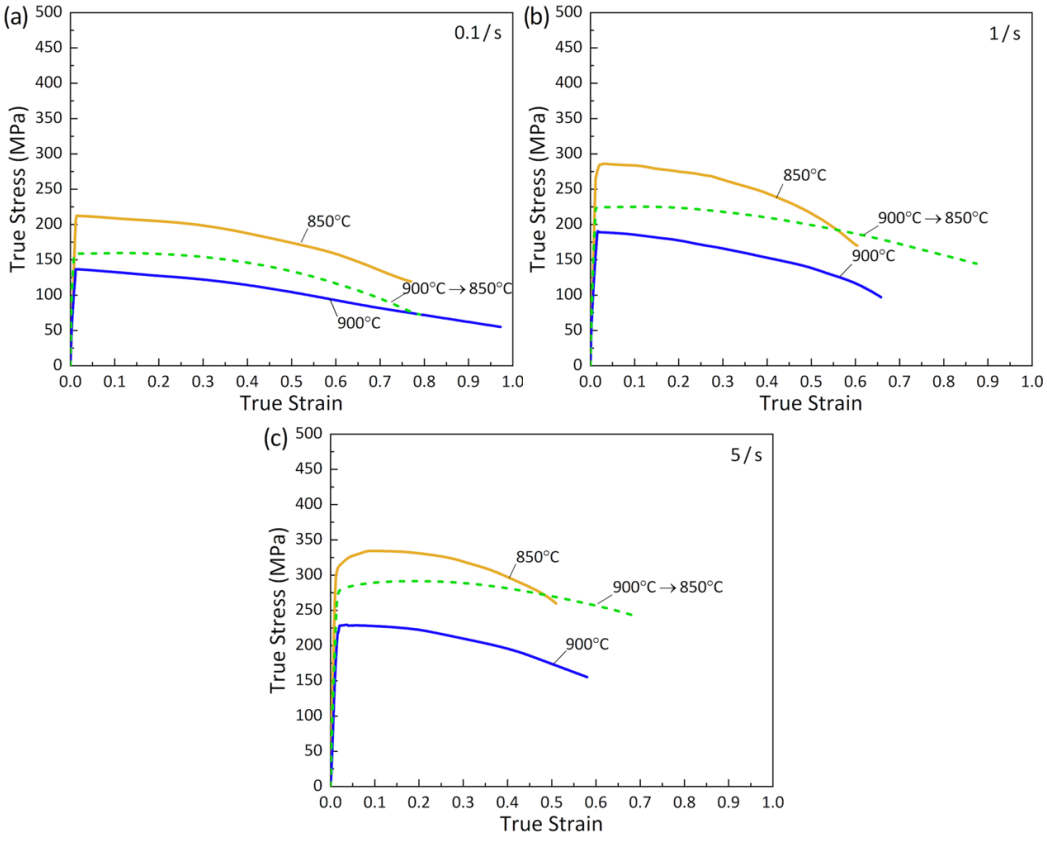


Figure 6. Comparison of true stress-strain curves after SQ at 900→850 °C and DH at 850 and 900 °C, at strain rates of (a) 0.1, (b) 1 and (c) 5 s^{-1}.

Figure 7 compares slopes fitted across the three nominal strain rates at reported true strains of 0.1 and 0.2. For the DH conditions shown, the fitted slopes increased with deformation temperature from 800 to 900 °C at both strains. The SQ950→800 °C slope decreased from 0.117 at strain 0.1 to 0.070 at strain 0.2, consistent with the decreasing stress separation between rates as the low-rate curve hardened and the higher-rate curves softened. The reported slopes for SQ900→850 °C were 0.156 at both strains, compared with 0.121 and 0.123 for DH850 °C.

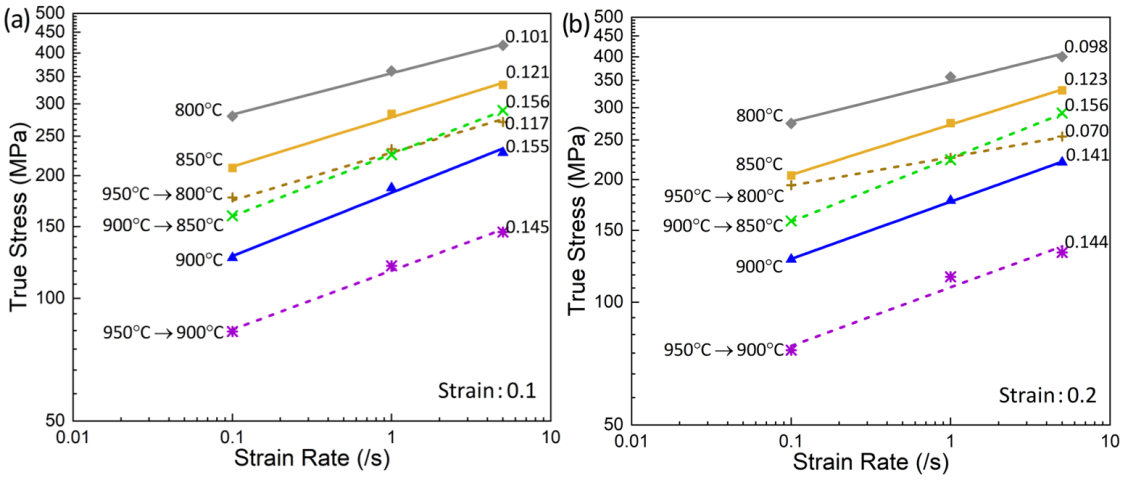


Figure 7. Apparent strain-rate sensitivity obtained from separate constant-rate tensile tests after DH and SQ, evaluated at true strains of (a) 0.1 and (b) 0.2.

Figure 8 compares the post-test microstructures of DH900 °C with SQ900→850 °C at three strain rates. For the SQ route, globular secondary α features were observed near primary α boundaries at 0.1 s^{-1}, were less apparent at 1 s^{-1}, and were not identified in the displayed 5 s^{-1} field. Compared with the microstructures following soaking at 950 °C in Figure 5, SQ900→850 °C showed a larger primary α population, consistent with the lower soaking temperature. Because DH900 °C and SQ900→850 °C also differ in deformation temperature, the differences between these two conditions reflect both the thermal route and the deformation condition.

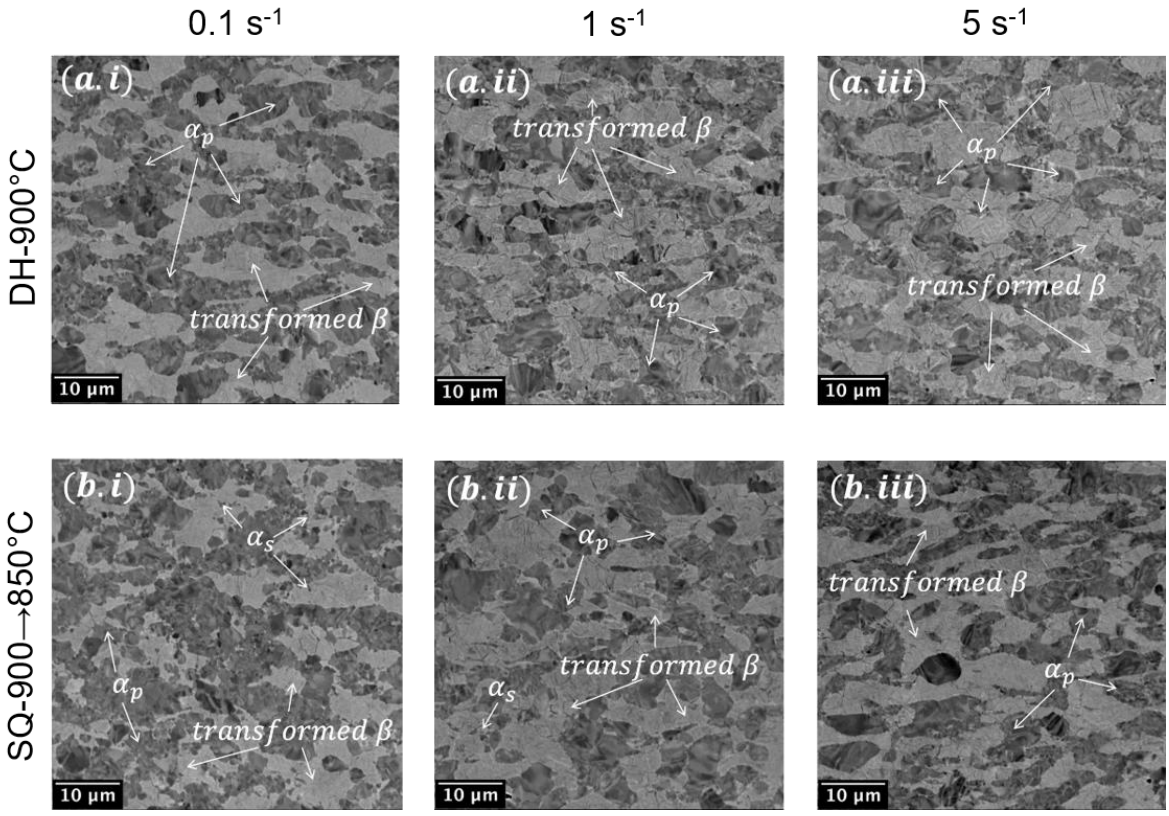


Figure 8. Post-test microstructures after (a) DH at 900 °C and (b) SQ at 900→850 °C, at strain rates of (i) 0.1, (ii) 1 and (iii) 5 s^{-1}.

Figure 9 compares the post-test α fractions for SQ950→900 °C, DH900 °C and SQ900→850 °C at different strain rates. Across the three thermal routes, the measured α fraction increased from SQ950→900 °C to DH900 °C and was highest at SQ900→850 °C. This trend is consistent with the different thermal exposures: the SQ950→900 °C specimens experienced a 950 °C soak before deformation at 900 °C, whereas the DH900 °C specimens remained at 900 °C, and the SQ900→850 °C specimens were cooled from 900 to 850 °C before deformation at the lower temperature. Within each thermal route, the measured α fraction decreased with increasing strain rate. Since increasing strain rate reduces the time spent deforming at the test temperature for a given strain, this trend is consistent with less time available for α evolution during deformation.

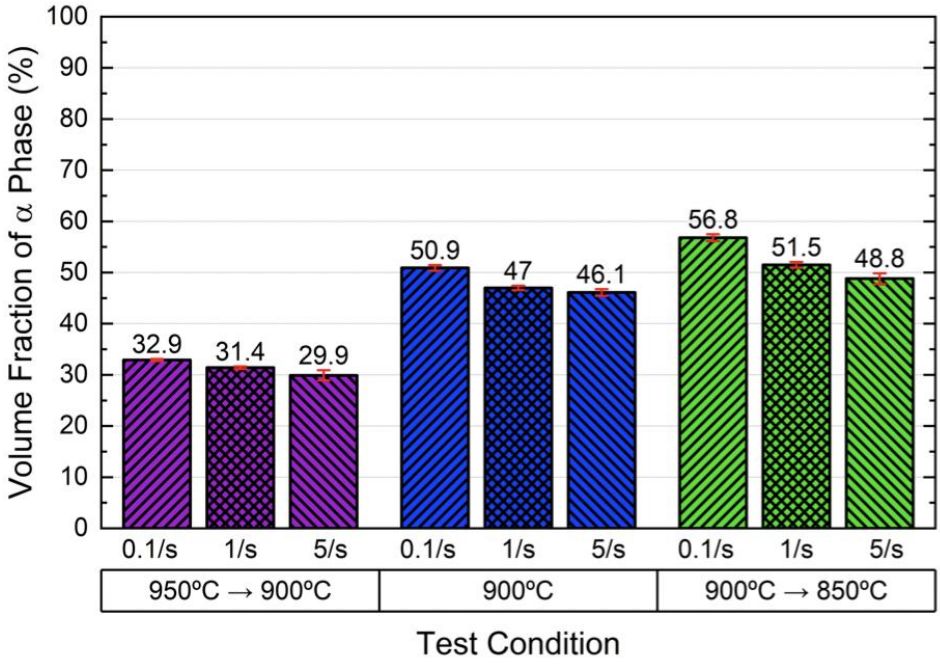


Figure 9. Reported post-test image-derived α (α_p + α_s) fractions for SQ950→900 °C, DH900 °C and SQ900→850 °C at 0.1, 1 and 5 s^{-1}. Error bars represent the standard deviations.

4 Constitutive description of thermal-history-dependent plasticity

4.1 Model framework and hardening response

The constitutive formulation combines a strain-hardening response and a plateau response with functions accounting for softening, phase evolution, strain-rate dependence and thermal history. It uses the mixture framework of Gavrus [39], and employs a generalised Voce hardening law [60]. Separate parameter sets are used for the DH and SQ conditions. The equivalent flow stress is expressed as:

$$\overline{\sigma} = (1-f)\left[wP\sigma_p + (1-wP)H\right]GF_{\text{th}} \tag{3}$$

Here, $\bar{\sigma}$ is the equivalent flow stress, ε is the accumulated equivalent plastic strain and $\dot{\varepsilon}$ is its rate. H and σ_p are the hardening and plateau stress responses, respectively, while f, w, P, G and F_{th} are dimensionless functions. The strain, strain-rate and thermal-history dependences in Equation 3 enter through its component functions. H and w evolve with accumulated plastic strain, while b, R_w and S_w depend on deformation temperature and strain rate through Equations 18-20. The damage-associated function f depends on strain, strain rate and temperature; G provides an explicit strain-rate contribution; P depends on the evolving phase-state variable; and F_{th} accounts for deformation temperature and the preceding soaking temperature. These functions are defined below.

The hardening branch is described using the generalised Voce form adopted from Gavrus [39][60]:

$$H = \sigma_0 + n_2[1 - \exp(-b\varepsilon)]^{n_3}, \qquad \sigma_p = \sigma_0 - n_1 \tag{4}$$

Here, σ_0 sets the initial level of the hardening response, n_2 defines its hardening increment and n_3 controls the shape of the hardening curve. The limiting value of H is $\sigma_0 + n_2$, while b controls the strain scale over which this value is approached. The plateau stress is $\sigma_p = \sigma_0 - n_1$. The temperature and strain-rate dependence of b is given in Equation 18. The transition between the hardening and plateau branches is controlled by the fitted softening weight w:

$$w = 1 - \exp(-R_w \varepsilon^{S_w}) \tag{5}$$

The coefficients R_w and S_w determine the evolution of this weight with strain and are functions of deformation temperature and strain rate, as defined in Equations 19 and 20. In the present formulation, w is used as a phenomenological softening variable rather than as a directly measured recrystallised fraction.

4.2 Phase transformation and thermal history

Step quenching separates the soaking temperature T_S from the deformation temperature T_D. The equilibrium α phase fraction is first estimated using the relation of Saby et al. [61]:

$$V_{\alpha,e}(T) = 0.92\{1 - \exp[-0.0085(T_\beta - T)]\} \tag{6}$$

where T_β is the β-transus temperature. $V_{\alpha,S}$ and $V_{\alpha,D}$ denote the corresponding equilibrium fractions evaluated at T_S and T_D, respectively. For the SQ route, the phase-associated α fraction during deformation is described using the modified Johnson-Mehl-Avrami type relation based on the Ti-6Al-4V transformation formulations [62][63]:

$$V_{\alpha,F} = V_{\alpha,S} + (V_{\alpha,D} - V_{\alpha,S})^{S_k}\left\{1 - \exp\left[-E\left(\frac{\varepsilon}{\dot{\varepsilon}}\right)^{F_{\mathrm{tr}}}\right]\right\} \tag{7}$$

with E and F_{tr} given by

$$E = E_0\left(\frac{V_{\alpha,D} - V_{\alpha,S}}{1 - V_{\alpha,D}}\right)^{V_e}, \qquad F_{\mathrm{tr}} = F_0\left(\frac{V_{\alpha,D} - V_{\alpha,S}}{1 - V_{\alpha,D}}\right)^{V_f} \tag{8}$$

The constants S_k, E_0, F_0, V_e and V_f control the phase-evolution function. For constant-rate loading from zero accumulated plastic strain, $\varepsilon/\dot{\varepsilon}$ represents the elapsed plastic-deformation time. The resulting phase term modifies the mixture weighting through:

$$P = \left[\frac{(1 - V_{\alpha,F})/V_{\alpha,F}}{(1 - V_{\alpha,\min})/V_{\alpha,\min}}\right]^I \tag{9}$$

where $V_{\alpha,\min}$ is the equilibrium α fraction at the highest soaking temperature of 950 °C and I is temperature dependent. For DH, $T_S = T_D$, and the phase-state variable is set to $V_{\alpha,F} = V_{\alpha,S} = V_{\alpha,D}$. For SQ, the distinction between T_S and T_D introduces the thermal-history dependence.

4.3 Damage and viscoplastic flow functions

Additional flow softening is represented by the phenomenological damage-associated function:

$$f = 1 - (1 - \beta \dot{\varepsilon}^{\eta} \varepsilon)^{\varphi} \tag{10}$$

Here, β, η and φ are temperature-dependent parameters defined in Equation 17. An explicit strain-rate contribution is introduced using the inverse-hyperbolic-sine form proposed by Gavrus [39]:

$$G = 1 + \operatorname{asinh}\left[\frac{1}{2}\left(\frac{\dot{\varepsilon}}{\dot{\varepsilon}_r}\right)^{C}\right] \tag{11}$$

where $\dot{\varepsilon}_r = 0.1\ s^{-1}$ and C is temperature dependent. Additional rate dependence also enters through b, R_w, S_w, f and the phase-state term. The effects of deformation temperature and the preceding soaking temperature are represented by:

$$F_{\text{th}} = \left[1 - D\left(\frac{T_S}{T_D}\right)^{n_x}\left(\frac{T_D - T_r}{T_m - T_r}\right)^{k}\right]^{m} \tag{12}$$

where $T_r = 293$ K and $T_m = 1904$ K. D and k are temperature-dependent parameters, whereas n_x and m are fitted constants. For DH, $T_S = T_D$ and Equation 12 reduces to the temperature-sensitivity form adopted from Liu et al [64]. For SQ, T_S/T_D introduces the additional thermal-history dependence.

4.4 Temperature dependence and material constants

The temperature-dependent coefficients are expressed using Arrhenius-type relations:

$$\sigma_0 = S_0 \exp\left(\frac{Q_s}{RT_D}\right), \quad n_1 = n_{10} \exp\left(-\frac{Q_{n1}}{RT_D}\right) \tag{13}$$

$$n_2 = n_{20} \exp\left(\frac{Q_{n2}}{RT_D}\right), \quad n_3 = n_{30} \exp\left(\frac{Q_{n3}}{RT_D}\right) \tag{14}$$

$$I = I_0 \exp\left(\frac{Q_I}{RT_D}\right), \quad C = C_0 \exp\left(-\frac{Q_C}{RT_D}\right) \tag{15}$$

$$k = k_0 \exp\left(\frac{Q_k}{RT_D}\right), \quad D = D_0 \exp\left(\frac{Q_D}{RT_D}\right) \tag{16}$$

$$\varphi = \varphi_0 \exp\left(\frac{Q_\varphi}{RT_D}\right), \quad \eta = \eta_0 \exp\left(\frac{Q_\eta}{RT_D}\right), \quad \beta = \beta_0 \exp\left(\frac{Q_\beta}{RT_D}\right) \tag{17}$$

The temperature- and strain-rate-dependent parameters b, R_w and S_w are given by:

$$b = b_0 \exp\left(\frac{Q_b}{RT_D}\right)\left(\frac{\dot{\varepsilon}}{\dot{\varepsilon}_r}\right)^{CF_b} \tag{18}$$

$$R_w = R_{w0} \exp\left(\frac{Q_{R_w}}{RT_D}\right)\left(\frac{\dot{\varepsilon}}{\dot{\varepsilon}_r}\right)^{CF_w} \tag{19}$$

$$S_w = S_{w0} \exp\left(\frac{Q_{S_w}}{RT_D}\right)\left(\frac{\dot{\varepsilon}}{\dot{\varepsilon}_r}\right)^{CF_w} \tag{20}$$

All temperatures are expressed in kelvin, R = 8.314 J mol^{-1} K^{-1}. The parameters Q are expressed in J mol^{-1}. Stress is evaluated in MPa, strain is dimensionless, strain rate is entered in s^{-1} and time in seconds, with $\dot{\varepsilon}_r$ = 0.1 s^{-1}. Phase fractions are expressed as fractions between zero and one rather than percentages.

The material constants were determined using the DH data and the SQ950→800 °C and SQ950→900 °C data over strain rates of 0.1-5 s^{-1}, with the fitting focused on plastic strains up to 0.2. A weighted objective function [65] and an evolutionary programming algorithm [66] were used for parameter identification. The SQ900→850 °C condition was subsequently used for an additional assessment of the fitted model. Separate DH and SQ parameter sets are listed in Table 4.

Table 4. Material constants used for the DH and SQ constitutive formulations.

Parameter	DH	SQ	Parameter	DH	SQ
φ_0	1.287	3.669	R_{w0}	1.869	1.801
Q_φ	5492.843	799.935	Q_{R_w}	3608.590	7785.842
β_0	0.003	0.063	S_{w0}	0.518	0.424
Q_β	41896.310	27981.020	Q_{S_w}	4076.074	3374.049
η_0	0.153	0.051	F_w	0.051	0.020
Q_η	2518.136	1734.657	C_0	6.472	4.174
S_0	82.882	82.053	Q_C	29782.665	22938.487
Q_s	8917.860	8884.007	S_k	0.520	0.520
n_{10}	79.363	46.154	E_0	0.568	0.568
n_{20}	0.561	0.031	V_e	2.356	2.356
n_{30}	0.010	0.008	F_0	0.417	0.417
Q_{n1}	4074.910	9920.579	V_f	0.230	0.230
Q_{n2}	49610.868	83274.090	I_0	0.534	0.534
Q_{n3}	45537.458	45645.401	Q_I	2618.354	2598.282
k_0	7.107	5.983	D_0	17.990	15.553
Q_k	3145.818	3963.258	Q_D	9489.468	8369.444
b_0	0.002	0.008	n_x	7.440	7.440
Q_b	58420.314	48001.560	m	4.882	4.789
F_b	2.159	0.702			

4.5 Model calibration and additional-route assessment

The constitutive formulation was first calibrated using the DH data and the SQ950→800 °C and SQ950→900 °C datasets described in the previous section. Figure 10a and 10b compare the experimental flow stresses with the corresponding fitted response surfaces. The formulation reproduces the main effects of deformation temperature, strain rate and strain on the measured flow response across these calibration conditions.

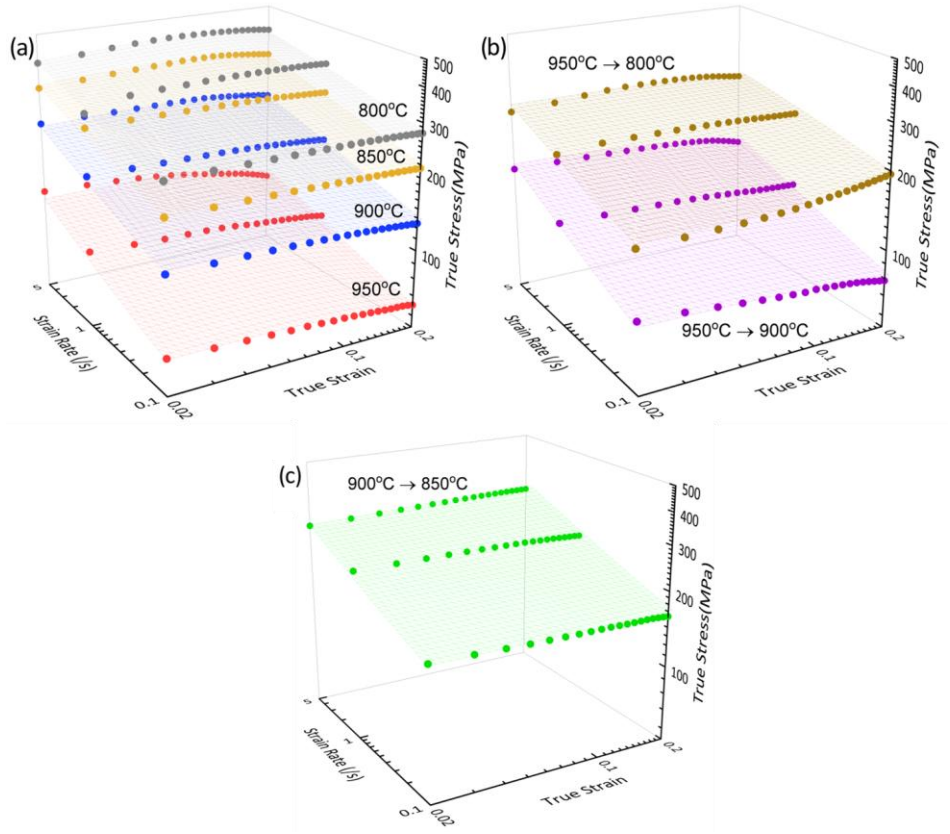


Figure 10. Comparison of experimental flow stresses (symbols) and constitutive-model response (surfaces) for (a) DH at 800–950 °C, (b) SQ950→800 °C and SQ950→900 °C calibration conditions, and (c) the additional SQ900→850 °C route, at nominal strain rates of 0.1-5 s^{-1}. Panels (a) and (b) correspond to data used for parameter identification; panel (c) assesses transfer of the SQ formulation to the selected lower-soaking-temperature route.

The SQ900→850 °C route was subsequently used to assess transfer of the SQ formulation to a lower soaking temperature and a smaller difference between soaking and deformation temperatures. The same SQ parameter set was applied without introducing a route-specific parameter set for this condition. As shown in Figure 10c, the original model calculation follows the overall stress level and rate dependence of the measured response over the strain range considered in the calibration. The comparison therefore indicates that the formulation can describe the principal flow characteristics of the selected 900→850 °C route within the investigated range.

The calibration and additional-route comparison show that the history-dependent formulation provides a common description of the DH and SQ tensile responses considered here. Its subsequent use in the forming simulation therefore employs the same constitutive structure and parameter sets established from the tensile programme.

5 Cup forming and component assessment

5.1 Cup forming

Figure 11a shows the cup components formed with draw ratios of 1.6, 1.7 and 1.8. No obvious necking or fracture was visible in the formed cups, consistent with the previously reported forming results [28]. The draw-ratio-1.8 cup was sectioned in the RD-ND plane. Figure 11b indicates the locations used for the location-specific analyses. Locations A-H follow the mid-thickness path from the cup bottom towards the upper wall/flange region, while d_i, d_c and d_o indicate inner, central and outer positions through the punch-corner thickness.

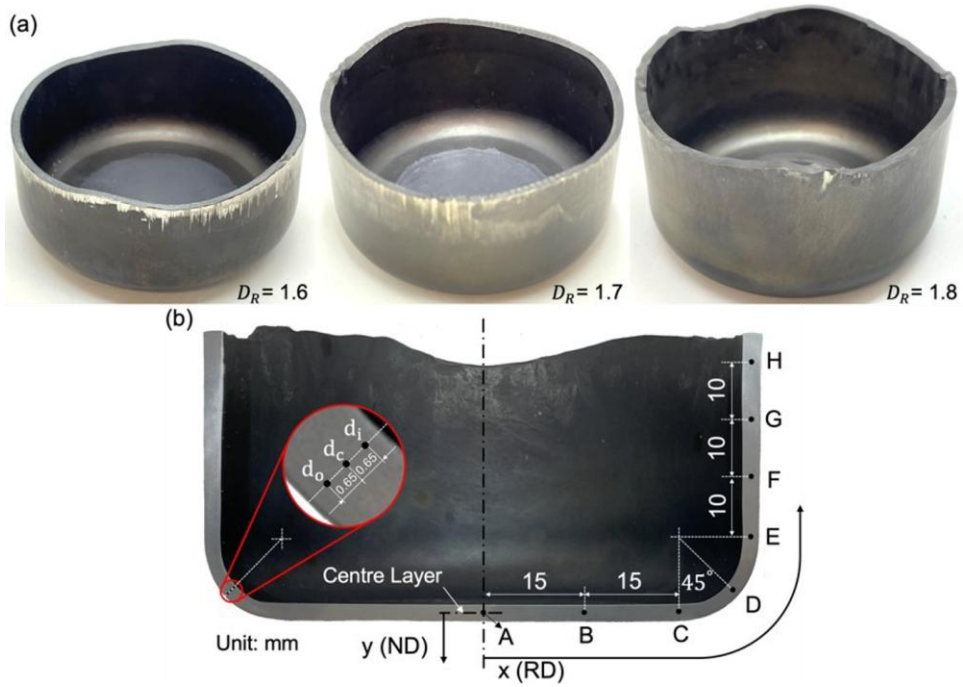


Figure 11. Ti-6Al-4V cup components formed after the 900→850 °C step-quenching route: (a) draw ratios of 1.6, 1.7 and 1.8; (b) half-section of the draw-ratio-1.8 cup showing the measurement locations. RD and ND denote the rolling and normal directions. Cup-forming feasibility was reported previously [28].

5.2 Predicted equivalent plastic strain distribution

Figure 12 shows the predicted equivalent plastic strain distribution across the cup half-section. The highest equivalent plastic strains were predicted in the upper wall/flange region. At the punch corner, the predicted equivalent plastic strain increased through the thickness from the inner surface to the outer surface. In the sidewall and close to the flange regions, the surface layers also experienced higher strain than the mid-thickness. This through-thickness variation is consistent with the bending, unbending and stretching experienced as the sheet passes through the die-entry region, which produces larger accumulated strains at the surfaces than near the mid-thickness.

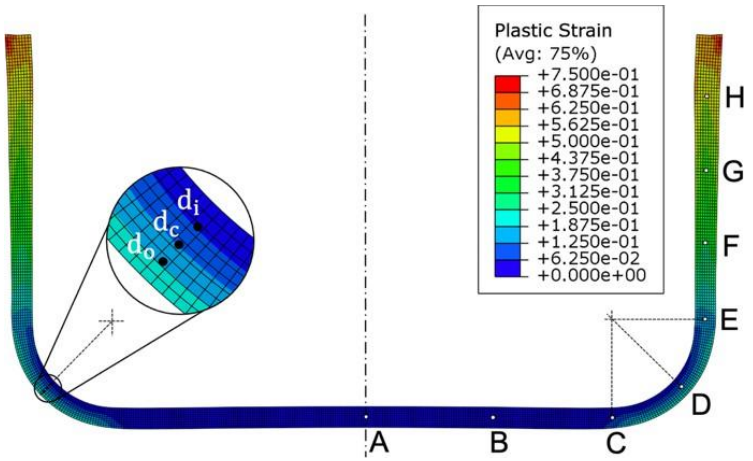


Figure 12. Predicted equivalent plastic strain distribution in the formed cup cross-section. A-H denote the same mid-thickness locations as in Figure 11.

Figure 13 quantifies the spatial variation shown in Figure 12. Along the mid-thickness path, the predicted equivalent plastic strain increased from 0.015 at A to 0.509 at H, with values of 0.122, 0.313 and 0.403 at D, F and G, respectively. Across the punch corner thickness, the strain increased from 0.071 at d_i to 0.122 at d_c and 0.180 at d_o. The predicted strains at F-H exceed the plastic-strain range up to 0.2 emphasised during constitutive calibration, and these higher-strain values should therefore be interpreted with appropriate caution.

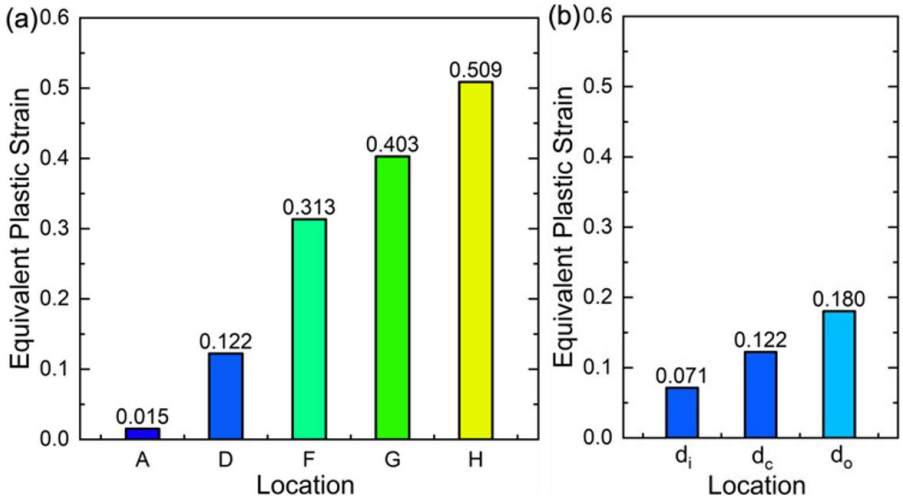


Figure 13. Predicted equivalent plastic strain at (a) selected mid-thickness locations A, D, F, G and H and (b) the inner, central and outer punch-corner positions d_i, d_c and d_o.

5.3 Component thickness

Figure 14 compares the measured and simulated normalised thickness profiles of the draw-ratio-1.8 cup. Thickness measurements were normalised by the initial blank thickness. The measured and simulated profiles show the same overall trend, although the simulation predicts less severe thinning near the punch corner. Only limited thinning occurred at the cup bottom, whereas the largest

measured thickness reduction, 12.7%, occurred between locations C and D near the punch corner. This region experiences bending under tension as the blank is drawn around the punch, which contributes to the local thinning [67][68]. Thickness subsequently increased towards the sidewall and flange, with the maximum measured thickening at the flange remaining below 20%. Comparison with the equivalent strain in Figures 12 and 13 also shows that local accumulated strain cannot be inferred from thickness change alone, particularly in regions affected by bending and unbending.

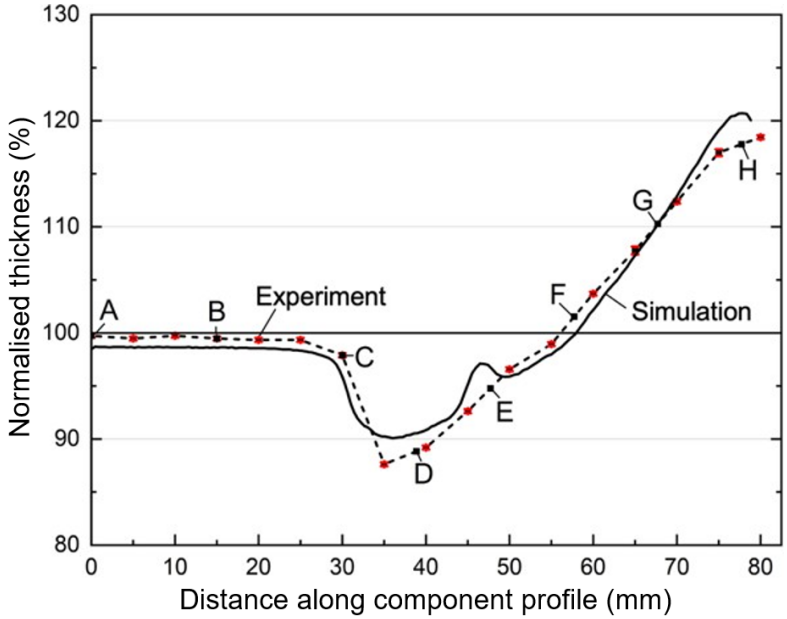


Figure 14. Measured and simulated normalised thickness profiles for the draw-ratio-1.8 cup after SQ900→850 °C. Normalisation is by the initial 2.56 mm thickness. The solid line denotes the simulation and the dashed line connects the experimental measurements.

5.4 Predicted temperature evolution during forming

Figure 15 shows the predicted temperature distribution at the start of forming and after 0.12 and 0.38 s. The blank was initially assigned a uniform temperature of 850 °C. By 0.12 s, the temperature field had become non-uniform. Plastic work dissipation produced local heating in the punch-corner and wall regions, with the highest temperature occurring near the outer surface around location D, while conductive heat transfer to the colder tooling reduced the temperature at contacting surfaces and in the flange region.

By 0.38 s, an evident through-thickness temperature gradient had developed around the punch corner, and the surfaces of the wall and flange were cooler than their interior. The predicted temperature evolution therefore shows that, even over the short forming interval, local heating from plastic

deformation and conductive cooling to the tools occur simultaneously. Consequently, deformation proceeds under a spatially varying temperature field rather than a uniform 850 °C condition.

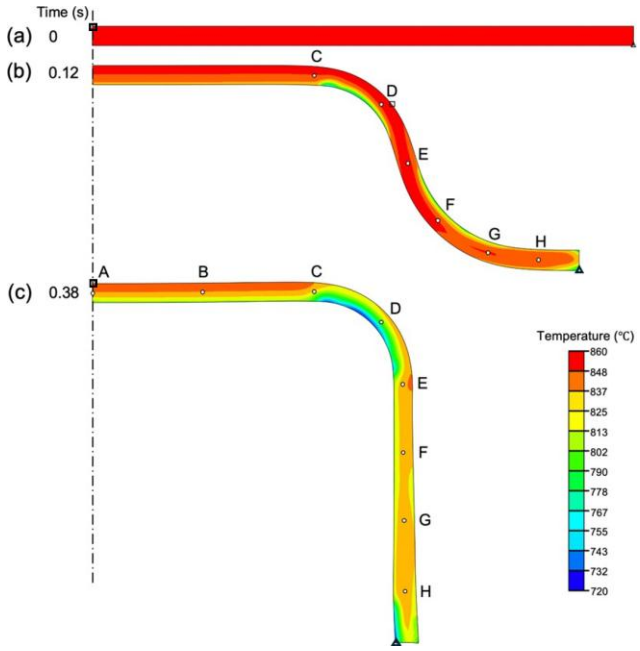


Figure 15. Predicted temperature distributions during forming at (a) 0 s, (b) 0.12 s and (c) 0.38 s. The squares and triangles mark the locations of the maximum and minimum temperatures, respectively.

5.5 Post-form microstructure

The post-forming microstructure comprised primary α grains and a transformed β constituent containing fine acicular α (Figure 16). The main phase constituents appeared broadly similar across the sampled locations and through-thickness positions, although differences in primary α morphology were evident. Primary α grains were predominantly equiaxed at the bottom; elongated grains were more evident in the wall and outer corner. The more elongated primary α morphology in the wall and outer corner is qualitatively consistent with the larger deformation predicted in these regions. The final microstructure reflects the combined effects of the preceding thermal route, deformation and subsequent cooling in contact with the tooling. The acicular α within the transformed constituent is consistent with transformation during cooling, although the post-forming micrographs do not resolve when this transformation occurred.

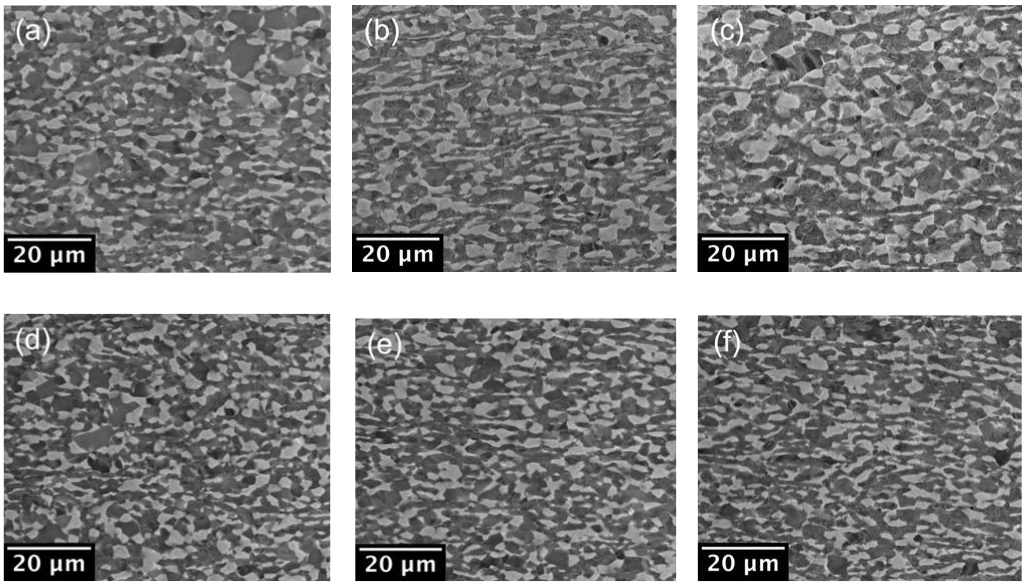


Figure 16. Post-forming BSE micrographs at (a) A, (b) F, (c) H, (d) inner corner layer d_i, (e) central corner layer d_c and (f) outer corner layer d_o. Primary α grains appear dark, whereas the transformed β constituent appears light.

6 Discussion

The tensile results show that the effect of step quenching cannot be judged from flow-stress reduction alone. Soaking at 950 °C followed by deformation at 800 or 900 °C reduced the stress relative to DH at the same deformation temperature, but the subsequent hardening and softening behaviour depended strongly on strain rate. In particular, SQ950→800 °C produced prolonged hardening at 0.1 s^{-1} while retaining substantial softening at higher rates. The SQ900→850 °C route reduced the flow stress relative to DH850 °C while maintaining less pronounced softening and a positive apparent rate dependence over the strain range examined. It therefore represents a practical compromise within the investigated matrix rather than a universal optimum.

The mechanical trends are consistent with the route-dependent post-test microstructures. The image-derived α fraction was lowest after SQ950→900 °C, higher after DH900 °C and highest after SQ900→850 °C, reflecting the different high-temperature exposures before and during deformation. Within each route, the measured α fraction decreased with increasing strain rate, consistent with the shorter time available for microstructural evolution. Globular secondary α features observed after SQ provide a possible link between phase evolution and the measured hardening/softening response, although the final microstructure also reflects subsequent cooling. Thermal history therefore influences both the phase state entering deformation and its evolution during loading.

The constitutive formulation provides a compact description of this history dependence. Separate DH and SQ parameter sets captured the calibration trends, while the same SQ formulation represented the principal stress and rate trends of the additional 900→850 °C route without introducing a route-specific parameter set. This supports transfer of the formulation across the thermal routes examined here. The calibration was focused on plastic strains up to 0.2, whereas the forming simulation predicted equivalent plastic strains above 0.3 in the wall and up to approximately 0.51 towards the upper wall/flange region. Quantitative interpretation of these higher-strain regions therefore extends beyond the strain range emphasised during tensile calibration.

At component level, the draw-ratio-1.8 cup showed limited thinning at the bottom and a maximum measured thickness reduction of 12.7% near the punch corner, followed by thickening towards the wall and flange. The simulation reproduced the overall thickness-profile trend but predicted less severe thinning at the punch corner. It also showed that the nominal 850 °C forming condition rapidly develops into a non-uniform temperature field because plastic-work heating and conductive cooling to the tools occur simultaneously. The spatial changes in primary α morphology after forming are qualitatively consistent with the heterogeneous deformation predicted across the cup. Together, these observations support the feasibility of the selected SQ900→850 °C route for rapid cup drawing. However, without a matched DH component, the present component results do not establish the magnitude of any forming advantage attributable specifically to step quenching.

7 Conclusions

The effects of subtransus thermal history on the rapid forming response of Ti-6Al-4V were examined through tensile testing, post-test microstructural characterisation, constitutive modelling and component-level assessment. The principal conclusions are:

1. Step quenching changed both the flow-stress level and the subsequent hardening/softening response at the same nominal deformation temperature. SQ950→800 °C produced prolonged hardening at 0.1 s^{-1}, whereas substantial softening remained at 5 s^{-1}. A reduction in initial flow stress alone therefore does not identify a favourable forming route.
2. SQ900→850 °C provided a favourable balance within the tested matrix, with a lower flow stress than DH850 °C, reduced softening over much of the measured strain range and positive apparent rate dependence. The fitted apparent rate-sensitivity slopes were 0.156 at reported strains of 0.1 and 0.2, compared with 0.121 and 0.123 for DH850 °C.
3. Post-test α morphology and image-derived α fractions varied systematically with thermal route and strain rate. The α fraction increased from SQ950→900 °C to DH900 °C and was

highest after SQ900→850 °C, while increasing strain rate reduced the measured α fraction within each route. These trends are consistent with the different thermal exposures and times available for microstructural evolution.

4. The thermal-history-dependent constitutive formulation captured the principal calibration trends for the DH and 950 °C-based SQ conditions and represented the additional SQ900→850 °C tensile response using the same SQ parameter set. The fitting was focused on plastic strains up to 0.2, while some regions of the component simulation extended beyond this strain range.
5. The previously demonstrated draw-ratio-1.8 cup [28] showed a maximum measured thickness reduction of 12.7% near the punch corner. The simulation captured the overall thickness-profile trend and predicted substantial spatial variations in equivalent plastic strain and temperature during the 0.38 s draw. The component results support forming feasibility for the selected SQ900→850 °C route, although comparison with a matched DH cup would be required to quantify any component-level advantage of step quenching.

Acknowledgements

The authors acknowledge funding from EPSRC under grant EP/R001715/1 and from the UKRI Impact Acceleration Account at Imperial College London under grant EP/X52556X/1. For the purpose of open access, the authors have applied a Creative Commons Attribution (CC BY) license to any Author Accepted Manuscript version arising.

CRediT authorship contribution statement

Famin Tian: Conceptualisation, Methodology, Investigation, Formal analysis, Validation, Visualisation, Writing - original draft. Hao Wu: Validation, Writing - review & editing. Nan Li: Conceptualisation, Supervision, Funding acquisition, Project administration, Writing - review & editing.

Data availability

The data supporting the findings of this study are available from the corresponding author on reasonable request.

Declaration of generative AI use

During the preparation of this work, the authors used ChatGPT (OpenAI) to assist with language editing, manuscript restructuring and literature checking. After using this tool, the authors reviewed, verified and edited the content as needed and take full responsibility for the content of the article.

References

[1] G. Lütjering, J.C. Williams, Engineering Materials and Processes, in: Titanium, 2nd ed., Springer Berlin, Heidelberg, 2007. https://doi.org/https://doi.org/10.1007/978-3-540-73036-1.

[2] C. Veiga, J.P. Davim, A.J.R. Loureiro, Properties and applications of titanium alloys: A brief review, Reviews on Advanced Materials Science 32 (2012).

[3] M. Peters, J. Kumpfert, C.H. Ward, C. Leyens, Titanium alloys for aerospace applications, Adv. Eng. Mater. 5 (2003). https://doi.org/10.1002/adem.200310095.

[4] F.H. Froes, M.N. Gungor, M.A. Imam, Cost-affordable titanium: The component fabrication perspective, JOM 59 (2007). https://doi.org/10.1007/s11837-007-0074-8.

[5] J.D. Beal, R. Boyer, D. Sanders, Forming of Titanium and Titanium Alloys, in: Metalworking: Sheet Forming, ASM International, 2006: pp. 656–669. https://doi.org/10.31399/asm.hb.v14b.a0005146.

[6] A.K. Ghosh, C.H. Hamilton, Influences of material parameters and microstructure on superplastic forming, Metallurgical Transactions A 13 (1982). https://doi.org/10.1007/BF02642386.

[7] A.K. Ghosh, C.H. Hamilton, Superplastic Sheet Forming, in: Metalworking: Sheet Forming, 2018. https://doi.org/10.31399/asm.hb.v14b.a0005147.

[8] J. Lin, Fundamentals of materials modelling for metals processing technologies: Theories and applications, 2015. https://doi.org/10.1142/P951.

[9] G. Bernhart, P. Lours, T. Cutard, V. Velay, F. Nazaret, Processes and equipment for superplastic forming of metals, in: Superplastic Forming of Advanced Metallic Materials: Methods and Applications, 2011. https://doi.org/10.1533/9780857092779.1.49.

[10] L. Hefti, Elevated Temperature Fabrication of Titanium Aerospace Components, Key Eng. Mater. 433 (2010) 49–55.

[11] B. Swale, M. Pizzingrilli, E. McCullagh, Superplastic Forming – Cost Effective, Key Eng. Mater. 433 (2010). https://doi.org/10.4028/scientific5/kem.433.41.

[12] Z. Hamedon, K.I. Mori, T. Maeno, Y. Yamashita, Hot stamping of titanium alloy sheet using resistance heating, 2013.

[13] K. Wang, M. Kopec, S. Chang, B. Qu, J. Liu, D.J. Politis, L. Wang, G. Liu, Enhanced formability and forming efficiency for two-phase titanium alloys by Fast light Alloys Stamping Technology (FAST), Mater. Des. 194 (2020). https://doi.org/10.1016/j.matdes.2020.108948.

[14] M. Kopec, K. Wang, D.J. Politis, Y. Wang, L. Wang, J. Lin, Formability and microstructure evolution mechanisms of Ti6Al4V alloy during a novel hot stamping process, Materials Science and Engineering: A (2018). https://doi.org/10.1016/j.msea.2018.02.038.

[15] N. Li, C. Sun, N. Guo, M. Mohamed, J. Lin, T. Matsumoto, C. Liu, Experimental investigation of boron steel at hot stamping conditions, J. Mater. Process. Technol. 228 (2016). https://doi.org/10.1016/j.jmatprotec.2015.09.043.

[16] M. Ganapathy, N. Li, J. Lin, D. Bhattacharjee, Investigation of a new hot stamping process with improved formability and productivity, in: Procedia Eng., 2017. https://doi.org/10.1016/j.proeng.2017.10.827.

[17] Z. Marciniak, K. Kuczyński, T. Pokora, Influence of the plastic properties of a material on the forming limit diagram for sheet metal in tension, Int. J. Mech. Sci. 15 (1973). https://doi.org/10.1016/0020-7403(73)90068-4.

[18] J.H. Sung, J.H. Kim, R.H. Wagoner, A plastic constitutive equation incorporating strain, strain-rate, and temperature, Int. J. Plast. 26 (2010). https://doi.org/10.1016/j.ijplas.2010.02.005.

[19] J.J. Jonas, R.A. Holt, C.E. Coleman, Plastic stability in tension and compression, Acta Metallurgica 24 (1976). https://doi.org/10.1016/0001-6160(76)90039-0.

[20] E. Alabort, D. Putman, R.C. Reed, Superplasticity in Ti-6Al-4V: Characterisation, modelling and applications, Acta Mater. 95 (2015). https://doi.org/10.1016/j.actamat.2015.04.056.

[21] E. Alabort, P. Kontis, D. Barba, K. Dragnevski, R.C. Reed, On the mechanisms of superplasticity in Ti-6Al-4V, Acta Mater. 105 (2016). https://doi.org/10.1016/j.actamat.2015.12.003.

[22] R. Ding, Z.X. Guo, A. Wilson, Microstructural evolution of a Ti-6Al-4V alloy during thermomechanical processing, Materials Science and Engineering: A 327 (2002). https://doi.org/10.1016/S0921-5093(01)01531-3.

[23] Q. Bai, J. Lin, T.A. Dean, D.S. Balint, T. Gao, Z. Zhang, Modelling of dominant softening mechanisms for Ti-6Al-4V in steady state hot forming conditions, Materials Science and Engineering: A 559 (2013). https://doi.org/10.1016/j.msea.2012.08.110.

[24] B. Guo, S.L. Semiatin, J.J. Jonas, Dynamic transformation during the high temperature deformation of two-phase titanium alloys, Materials Science and Engineering: A 761 (2019). https://doi.org/10.1016/j.msea.2019.138047.

[25] J.Y. Kim, K.T. Park, I.O. Shim, S.H. Hong, Globularization behavior of ELI grade Ti-6A1-4V alloy during non-isothermal multi-step forging, Mater. Trans. 49 (2008). https://doi.org/10.2320/matertrans.MER2007224.

[26] S.L. Semiatin, T.R. Bieler, Effect of texture and slip mode on the anisotropy of plastic flow and flow softening during hot working of Ti-6Al-4V, Metall. Mater. Trans. A Phys. Metall. Mater. Sci. 32 (2001). https://doi.org/10.1007/s11661-001-0155-1.

[27] F. Tian, N. Li, Investigation of the feasibility of a novel heat stamping process for producing complex-shaped Ti-6Al-4V panel components, in: Procedia Manuf., 2020. https://doi.org/10.1016/j.promfg.2020.04.267.

[28] H. Wu, F. Tian, C. Tang, Z. Guo, N. Li, Novel Heat Stamping of Ti6Al4V panels with high drawability and low springback, MATEC Web of Conferences 401 (2024). https://doi.org/10.1051/matecconf/202440101012.

[29] J. Xiao, D.S. Li, X.Q. Li, T.S. Deng, Constitutive modeling and microstructure change of Ti-6Al-4V during the hot tensile deformation, J. Alloys Compd. 541 (2012). https://doi.org/10.1016/j.jallcom.2012.07.048.

[30] V. Velay, H. Matsumoto, V. Vidal, A. Chiba, Behavior modeling and microstructural evolutions of Ti-6Al-4V alloy under hot forming conditions, Int. J. Mech. Sci. 108–109 (2016). https://doi.org/10.1016/j.ijmecsci.2016.01.024.

[31] S. Gao, Y. Sang, Q. Li, Y. Sun, Y. Wu, H. Wang, Constitutive modeling and microstructure research on the deformation mechanism of Ti-6Al-4V alloy under hot forming condition, J. Alloys Compd. 892 (2022). https://doi.org/10.1016/j.jallcom.2021.162128.

[32] P. Martin, A. Prillieux, Y. Balcaen, A. Hacquin, M. Saby, B. Dod, J. Alexis, S. Perusin, Rheology of Ti-6Al-4V alloy under non equilibrium conditions during β forging, J. Mater. Process. Technol. 327 (2024). https://doi.org/10.1016/j.jmatprotec.2024.118346.

[33] Z. Gao, S. Liu, J. Lin, Z. Wang, D. Li, K. Zheng, Development of Viscoplastic Constitutive Model Considering Heating Rate Effect on Grain Size and Phase Evolution in Hot Deformation, Materials 18 (2025). https://doi.org/10.3390/ma18143251.

[34] Z. Cai, J. Chen, Y. Liu, H. Mei, G. Ma, X. Li, Y. Li, Unified modeling of deformation and properties for multi-stage hot forming with complex thermo-mechanical histories: Application to complex hollow titanium alloy components, J. Mater. Process. Technol. 356 (2026). https://doi.org/10.1016/j.jmatprotec.2026.119465.

[35] G.R. Johnson, W.H. Cook, A constitutive model and data for metals subjected to large strains, high strain rates and high temperatures. The 7th International Symposium on Ballistics, in: Proceedings of the 7th International Symposium on Ballistics, 1983.

[36] Y.C. Lin, X.M. Chen, A critical review of experimental results and constitutive descriptions for metals and alloys in hot working, Mater. Des. 32 (2011). https://doi.org/10.1016/j.matdes.2010.11.048.

[37] A.S. Khan, R. Liang, Behaviors of three BCC metal over a wide range of strain rates and temperatures: Experiments and modeling, Int. J. Plast. 15 (1999). https://doi.org/10.1016/S0749-6419(99)00030-3.

[38] A.S. Khan, Y.S. Suh, R. Kazmi, Quasi-static and dynamic loading responses and constitutive modeling of titanium alloys, Int. J. Plast. 20 (2004). https://doi.org/10.1016/j.ijplas.2003.06.005.

[39] A. Gavrus, Constitutive equation for description of metallic materials behavior during static and dynamic loadings taking into account important gradients of plastic deformation, in: Key Eng. Mater., 2012. https://doi.org/10.4028/www.scientific.net/KEM.504-506.697.

[40] F. Tian, Development of a new heat stamping process for titanium alloy panel components, Imperial College London, 2023.

[41] B. Pan, D. Wu, Z. Wang, Y. Xia, High-temperature digital image correlation method for full-field deformation measurement at 1200 °C, Meas. Sci. Technol. 22 (2011). https://doi.org/10.1088/0957-0233/22/1/015701.

[42] G. Crammond, S.W. Boyd, J.M. Dulieu-Barton, Speckle pattern quality assessment for digital image correlation, Opt. Lasers Eng. 51 (2013). https://doi.org/10.1016/j.optlaseng.2013.03.014.

[43] X. Guo, J. Liang, Z. Tang, B. Cao, M. Yu, High-temperature digital image correlation method for full-field deformation measurement captured with filters at 2600°C using spraying to form speckle patterns, Optical Engineering 53 (2014). https://doi.org/10.1117/1.oe.53.6.063101.

[44] M.S. Nixon, A.S. Aguado, Low-level feature extraction (including edge detection), in: Feature Extraction and Image Processing for Computer Vision, 2026. https://doi.org/10.1016/b978-0-443-36686-4.00013-4.

[45] S.W. Smith, Moving Average Filters, in: Digital Signal Processing: A Practical Guide for Engineers and Scientists, Elsevier, 2003: pp. 277–284.

[46] L. Ming, O. Pantalé, An efficient and robust VUMAT implementation of elastoplastic constitutive laws in Abaqus/Explicit finite element code, Mechanics and Industry 19 (2018). https://doi.org/10.1051/meca/2018021.

[47] Q. Bai, Development of a New Process for High Precision Gas Turbine Blade Forging, Imperial College London, 2012.

[48] T. Mukherjee, W. Zhang, T. DebRoy, An improved prediction of residual stresses and distortion in additive manufacturing, Comput. Mater. Sci. 126 (2017). https://doi.org/10.1016/j.commatsci.2016.10.003.

[49] S. Ivanov, M. Gushchina, A. Artinov, M. Khomutov, E. Zemlyakov, Effect of elevated temperatures on the mechanical properties of a direct laser deposited ti-6al-4v, Materials 14 (2021). https://doi.org/10.3390/ma14216432.

[50] D. Rittel, L.H. Zhang, S. Osovski, The dependence of the Taylor–Quinney coefficient on the dynamic loading mode, J. Mech. Phys. Solids 107 (2017). https://doi.org/10.1016/j.jmps.2017.06.016.

[51] X. Liu, M. Kopec, O. El Fakir, H. Qu, Y. Wang, L. Wang, Z. Li, Characterisation of the interfacial heat transfer coefficient in hot stamping of titanium alloys, International Communications in Heat and Mass Transfer 113 (2020). https://doi.org/10.1016/j.icheatmasstransfer.2020.104535.

[52] S.L. Semiatin, V. Seetharaman, I. Weiss, Hot workability of titanium and titanium aluminide alloys - An overview, Materials Science and Engineering: A 243 (1998). https://doi.org/10.1016/s0921-5093(97)00776-4.

[53] K. Wang, M.Q. Li, Morphology and crystallographic orientation of the secondary α phase in a compressed α/β titanium alloy, Scr. Mater. 68 (2013). https://doi.org/10.1016/j.scriptamat.2013.02.048.

[54] K. Wang, M.Q. Li, Effects of heat treatment and hot deformation on the secondary α phase evolution of TC8 titanium alloy, Materials Science and Engineering: A 613 (2014). https://doi.org/10.1016/j.msea.2014.06.056.

[55] M. Meng, X.G. Fan, H. Yang, L.G. Guo, M. Zhan, P.F. Gao, Precipitation of secondary alpha in competition with epitaxial growth of primary alpha in two-phase titanium alloys, J. Alloys Compd. 714 (2017). https://doi.org/10.1016/j.jallcom.2017.04.209.

[56] W. Yu, M.Q. Li, J. Luo, Effect of deformation parameters on the precipitation mechanism of secondary α phase under high temperature isothermal compression of Ti-6Al-4V alloy, Materials Science and Engineering: A 527 (2010). https://doi.org/10.1016/j.msea.2010.03.024.

[57] B. Babu, L.E. Lindgren, Dislocation density based model for plastic deformation and globularization of Ti-6Al-4V, Int. J. Plast. 50 (2013). https://doi.org/10.1016/j.ijplas.2013.04.003.

[58] Y.Q. Ning, X. Luo, H.Q. Liang, H.Z. Guo, J.L. Zhang, K. Tan, Competition between dynamic recovery and recrystallization during hot deformation for TC18 titanium alloy, Materials Science and Engineering: A 635 (2015). https://doi.org/10.1016/j.msea.2015.03.071.

[59] A.S. Khan, S. Yu, Deformation induced anisotropic responses of Ti-6Al-4V alloy. Part I: Experiments, Int. J. Plast. 38 (2012). https://doi.org/10.1016/j.ijplas.2012.03.015.

[60] A. Gavrus, Formulation of a new constitutive equation available simultaneously for static and dynamic loadings, in: DYMAT 2009 - 9th International Conference on the Mechanical and Physical Behaviour of Materials under Dynamic Loading, EDP Sciences, 2009: pp. 1239–1244. https://doi.org/https://doi.org/10.1051/dymat/2009174.

[61] M. Saby, E. Massoni, N. Bozzolo, A metallurgical approach to individually assess the rheology of alpha and beta phases of Ti-6Al-4V in the two-phase domain, Mater. Charact. 89 (2014). https://doi.org/10.1016/j.matchar.2014.01.001.

[62] S. Malinov, P. Markovsky, W. Sha, Z. Guo, Resistivity study and computer modelling of the isothermal transformation kinetics of Ti-6Al-4V and Ti-6Al-2Sn-4Zr-2Mo-0.08Si alloys, J. Alloys Compd. 314 (2001). https://doi.org/10.1016/S0925-8388(00)01227-5.

[63] S. Malinov, Z. Guo, W. Sha, A. Wilson, Differential scanning calorimetry study and computer modeling of β ⇒ α phase transformation in a Ti-6Al-4V alloy, Metallurgical and Materials Transactions A 32 (2001) 879–887. https://doi.org/https://doi.org/10.1007/s11661-001-0345-x.

[64] S. Liu, A. Kouadri-Henni, A. Gavrus, Numerical simulation and experimental investigation on the residual stresses in a laser beam welded dual phase DP600 steel plate: Thermo-mechanical

material plasticity model, Int. J. Mech. Sci. 122 (2017). https://doi.org/10.1016/j.ijmecsci.2017.01.006.

[65] J. Cao, J. Lin, A study on formulation of objective functions for determining material models, Int. J. Mech. Sci. 50 (2008). https://doi.org/10.1016/j.ijmecsci.2007.07.003.

[66] B. Li, J. Lin, X. Yao, A novel evolutionary algorithm for determining unified creep damage constitutive equations, Int. J. Mech. Sci. 44 (2002). https://doi.org/10.1016/S0020-7403(02)00021-8.

[67] V.D. Luiz, P.C. De Matos Rodrigues, Design of a tribo-simulator for investigation of the tribological behavior of stainless-steel sheets under different contact conditions, Materials Research 25 (2022). https://doi.org/10.1590/1980-5373-MR-2021-0220.

[68] E. Ceron, P.A.F. Martins, N. Bay, Thermal analysis of bending under tension test, in: Procedia Eng., 2014. https://doi.org/10.1016/j.proeng.2014.10.236.